An overview of aerosol properties in clear and cloudy sky based on the CALIPSO observations

Yulan Hong[a], Larry Di Girolamo[a]

a. Department of Atmospheric Sciences, University of Illinois at Urbana-Champaign, Urbana, Illinois, USA

Correspondence: Yulan Hong (yulanh@illinois.edu)

Key Points:

- The study reveals that the below-cloud aerosols may share similar properties with those without clouds overlying.
- The wide coverage of the below-cloud aerosols indicates the significance of cirrus's impact on aerosol direct radiative effect.
- Regional and seasonal variations of the cloud-free and cloudy aerosols strongly depend on local climate system and long-track transport.

Abstract

A full understanding of the climatological properties of aerosols is an important step towards characterizing their effects on the regional and global climate. Utilizing the observations from Cloud-Aerosol Lidar and Infrared Pathfinder Satellite Observations (CALIPSO), we study cloud-free and cloudy aerosol properties with attentions on aerosol and cloud layer vertically relative positions. On a global scale, the cloud-free aerosols account for 55.9% of all detected aerosols with a mean optical depth ($\bar{\tau}_a$) and uncertainty of 0.135 ± 0.047. The cloudy aerosols, accounting for 44.1%, have a larger $\bar{\tau}_a$ and uncertainty of 0.143 ± 0.074 compared to the cloud-free aerosols. The above-cloud aerosols (4.2%), primarily composed of elevated smoke, dust/volcanic ash and polluted dust, have a much smaller $\bar{\tau}_a$ (0.056$\pm$0.038). The below-cloud aerosols (21.3%) have $\bar{\tau}_a$~ 0.165$\pm$ 0.087, showing close τ_a probability density distributions, aerosol types, backscatter-depolarization ratio diagram, and lidar ratio-color ratio diagram with the cloud-free aerosols. In addition, 27.4% of the detected aerosol profiles are found to have cloud layers vertically connected to aerosol layers. The lidar backscatter profiles of these aerosols have larger median values than the cloud-free, above-cloud and below-cloud aerosols. The seasonal variability of the cloud-free and the cloudy aerosols significantly varies with regions. This study implies that quantifying the impact of clouds, particularly cirrus due to the wide coverage of cirrus-aerosol overlap, on aerosol direct radiative effect is crucial to assess aerosols' roles in the Earth-climate system.

1. Introduction

Aerosols impact on Earth weather and climate system by their direct and indirect effects, which has been intensely studied in the past few years (Andreae & Rosenfeld, 2008; Chand et al., 2009; Ten Hoeve & Augustine, 2016; Lohmann & Feichter, 2005; Matus et al., 2015; Rosenfeld et al., 2014; Tan et al., 2017). According to the most recent Intergovernmental Panel on Climate Change (IPCC) report, the radiative forcing due to aerosols from observation-based evidence was assessed to be -0.4 $\pm$ 0.4 W m^{-2} (IPCC, 2021), which is likely able to offset part of the warming induced by the emission of greenhouse gases (Rosenfeld et al., 2019), but with the uncertainty in the same order as the estimated value.

Whether aerosols directly warm or cool locally not only depends on aerosol physical and chemical properties but only relies on the properties of the vertically overlapping clouds. For instance, biomass burning aerosols can switch from a net cooling to a net warming effect at the top of atmosphere (TOA) with an increase of underlying cloud fraction (Chand et al., 2009; Keil & Haywood, 2003). Similarly, increase of underlying cloud fraction and optical depth was found to enhance the warming effect of dust aerosols (Xu et al., 2017). A cirrus layer overlying an aerosol layer is able to cause modest change of the radiative effect of absorbing or nonabsorbing aerosols at TOA (Liao & Seinfeld, 1998). Considering the wide coverage of cirrus clouds globally (Hong & Liu, 2015), cirrus impact on aerosol direct radiative effect could be extraordinary, which by now has not been assessed over the globe.

Incomplete knowledge of cloud-aerosol interactions also challenges an accurate estimate of aerosol direct radiative effect. Cloud active aerosols indirectly interact with clouds by modifying cloud microstructure such as reducing liquid cloud effective radius (Ross et al., 2018; Tan et al., 2017), suppressing precipitation (Andreae & Rosenfeld, 2008; Rosenfeld et al., 2014), increasing cloud cover in precipitating clouds or the opposite in non-precipitating clouds

(Christensen & Stephens, 2011; Lebsock et al., 2008). These effects in turn modify aerosol direct radiative effect with the extent of modification depending on cloud-aerosol relative positioning in the atmosphere. Nevertheless, the fundamental understanding of aerosol-cloud-precipitation interactions and their representation in large-scale models is insufficient. For instance, IPCC AR6 reports that the total aerosol forcing including aerosol-radiation and aerosol-cloud interaction vary widely between different climate models from -1.50 to -0.68 W m^{-2} (IPCC, 2021).

Additionally, clouds modify aerosol properties. For instance, aerosols exposed near cloud edge were found with the lidar backscatter and extinction coefficient enhanced resulted from humidification effects on aerosol properties (Rauber et al., 2013; Tackett & Di Girolamo, 2009). While aerosol loading above low-level cloud top is posited to have no significant difference with adjacent clear sky over the Southeast Atlantic according to the ORACLES (ObseRvations of Aerosols above Clouds and their intEractionS) filed campaign data (Shinozuka et al., 2020). However, Chung et al., (2016) stated that aerosol optical depth (AOD or τ_a) above low-level cloud is generally smaller than clear sky in the nearby over the globe as showed by the CALIPSO observations. The disagreement between these two studies indicates how clouds modify aerosol properties near cloud top locally or globally is not clear. This incomplete knowledge also posts challenges in reducing the uncertainties in aerosol radiative effects.

Characterizing the amount and distribution of aerosols and their co-occurrence with clouds from observations is an important step to improve the estimate of aerosol direct and indirect effects on the Earth climate system. Global or regional aerosol climatologies which show aerosol loadings, seasonal variations, land-sea contrast derived from passive sensors have been displayed in a series of studies (Kim et al., 2007; Mao et al., 2014; Mehta et al., 2016; Mishchenko et al., 2007). These climatologies represent the cloud-free aerosols, which has been applied for a wide range of purposes, such as assessment of their effects on climate (Loeb & Manalo-Smith, 2005) or model evaluation (Palacios-Penã et al., 2019). A climatology only considering the clear-sky aerosols could be biased if aerosols occurring in cloudy sky significantly differ from those in clear sky.

Active sensors probing into atmosphere with cloud and aerosol vertical structures resolved are able to detect aerosols in cloudy sky. For instance, by utilizing the CALIPSO lidar, aerosol and cloud layers are decoupled, and a 3-D aerosol climatology have been derived in both clear and cloudy skies (Winker et al., 2013). Also, attentions have been paid to the global distributions of the above-cloud aerosols with the help of the CALIPSO observations (Alfaro-Contreras et al., 2016; Devasthale & Thomas, 2011). Insufficient studies target to the aerosols appearing below clouds detected from space with the concern of the lidar signal attenuation and additional uncertainty induced from the cloud layers (Chung et al., 2016; Tackett & Di Girolamo, 2009). The CALIPSO aerosol algorithm has considered appropriate signal correction through first retrieving the overlying layers and then using the retrieved attenuation for the attenuation correction below (Winker et al., 2009).

In this study, using the CALIPSO observations, our main objective is to characterize the properties of aerosols in clear and cloudy skies with their uncertainties considered. The distributions of cloudy aerosols are studied by considering the relative positions of cloud and aerosol layers. Overall, we focus on the following scientific questions:

1. How the spatial distributions of the aerosols occurring above, below or vertically adjunct to clouds differ from the cloud-free aerosols;

2. What are the optical properties and lidar parameters for the aerosols above, below or adjunct to cloud layers and the cloud-free aerosols;
3. What are the differences in the regional and seasonal variabilities of the cloudy and the cloud-free aerosols.

2. Data and Methodology

2.1 CALIPSO

CALIPSO launched in April 2006 carries three primary instruments: the Imaging Infrared Radiometer (IIR), the Wide Field Camera (WFC) and the near-nadir view Cloud-Aerosol Lidar with Orthogonal Polarization (CALIOP). The CALIOP operates at three channels measuring the backscatter data at 1064 nm and the two orthogonal polarization components at 532 nm that provide near global measurements of aerosol and cloud profiles (Winker et al., 2003). The CALIPSO level 2 dataflow starts from a search of atmospheric features (cloud or aerosol layers) utilizing the 532 nm attenuated backscatter profiles (Vaughan et al., 2009). The scene classification algorithm (SCA) identifies the atmospheric features as clouds (liquid or ice) or aerosols (aerosol types) (Liu et al., 2009). Profiles of extinction coefficients and particle backscatter are retrieved within the layers by the hybrid extinction retrieval algorithm (HERA) (Winker et al., 2009; Young & Vaughan, 2009).The retrieved profiles are compiling into the profile products, while the layer products report the layer top and base, integrated optical properties, etc. Regions with low loadings of aerosols that undergo undetected by CALIOP are reported as 'clear air', which are assigned to zero extinction coefficient (Winker et al., 2009).

The CALIPSO level 2 aerosol and cloud merged layers product, version 4-20 (CAL_LID_L2_05kmMLay-Standard-V4-20) is the main dataset used in this study. This merged layer product reports column properties of aerosol and cloud in 5-km resolution, including layer top and base altitude, integrated attenuated backscatter, volume depolarization ratio, color ratio, optical depth and the corresponding uncertainties calculated based on error propagation (Winker et al., 2009; Young et al., 2008, 2013). A CAD (cloud and aerosol discrimination) score is also reported for each layer, which adopts lidar backscatter, color ratio, and altitude to produce a possibility for discriminating cloud and aerosol (Liu et al., 2009, 2019). The CAD score also represents a confidence level for cloud and aerosol classification with larger absolute values for a higher confidence. The level 2 aerosol profile product (CAL_LID_L2_05kmAPro-Standard-V4-20) is also used to obtain the lidar backscatter profiles at 532 nm for our climatology study. Data from 2007.01-2020.06 is used for this work. Table 1 summarizes the data products and variables used in this study.

Table 1. Data products and the corresponding variables used in this study.

Product	Variables
CAL_LID_L2_05kmMLay-Standard-V4-20	Column_Optical_Depth_Tropospheric_Aerosols_532
	Column_Opitcal_Depth_Troposperic_Aerosols_Uncertainty_532
	CAD_Score
	Layer_Top_Altitude
	Layer_Base_Altitude
	ExtinctionQC_532
	Integrated_Attenuated_Backscatter_532
	Integrated_Volume_Depolarization_Ratio
	Final_532_Lidar_Ratio

	Integrated_Attenuated_Total_Color_Ratio Day_Night_Flag IGBP_Surface_Type Minimum_Laser_Energy_532 Latitude Longitude
CAL_LID_L2_05kmAPro-Standard-V4-20	Total_Backscatter_Coefficient_532

2.2 Data Quality Control

CALIOP is experiencing low energy laser shots above the South Atlantic Anomaly (SAA) region since 2016. To exclude those low energy shots, profiles containing 532 nm laser energy less than 80 mJ are not considered as recommended by the CALIPSO team (https://www-calipso.larc.nasa.gov/resources/calipso_users_guide/advisory/advisory_2018-06-12/CALIPSO_Laser_Energy_Technical_Advisory.pdf). Similar to Tackett et al. (2018) and Winker et al. (2013) , our study also applies several filters to the CALIPSO data to ensure data quality. The data passing the filters must meet the following criterions. First, the CAD scores must be in the range of -100 to -20, representing intermediate to high confidence levels -- CAD filter; second, extinction_QC_flag_532 values are equal to either 0 (unconstrained retrieval; initial lidar ratio unchanged during solution process), or 1 (constrained retrieval), or 16 (opaque layers and unchanged lidar ratio), or 18 (opaque layers and changed lidar ratio) – Ext_QC filter; third, aerosol layer above 4 km should not be adjunct to clouds which may be misclassified from cirrus fringes – Ci filter. Note that when a column has one aerosol layer being filtered, the whole column will be excluded in our analysis. As summarized in Table 2, aerosols in cloudy sky are influenced by the filters more than in clear sky. The Ext_QC filter modifies the most on AOD compared to other filters.

Table 2. Summary of global mean aerosol optical depth with different filters applied.

	All filters	No CAD filter	No Ci filter	No Ext_QC filter
Cloud-free	0.135	0.138	0.135	0.157
Cloudy	0.143	0.159	0.141	0.209
All aerosol	0.139	0.148	0.138	0.180

2.3 Classification of Aerosols

Figure 1 shows how we group the detected aerosols (i.e. those aerosols with $\tau_a > 0$) for a better characterization of aerosols in cloudy sky. The quality-controlled aerosol data is divided into two main groups based on cloud presence: cloud-free and cloudy aerosols. In each cloudy sky profile, by checking the gap of the closest aerosol and cloud layer, we deduce whether there are any aerosol and cloud layers vertically connected. If the gap is less than 0.5 km, the profile will be classified as *connected-cloud* aerosol (Figure 1b), otherwise, it will be grouped as *isolated-cloud* aerosol (Figure 1c). According to the vertically relative locations of aerosol and cloud layers, the *connected-cloud* aerosols have four subcategories. When there is only one aerosol and one cloud layer in the column and they are vertically connected, this profile is classified as the *one-layer aerosol-cloud connected* group. The aerosol layer can be above or/and below cloud layer. An example is shown in Figure 1b1. The second group of the connected-cloud aerosol is *aerosol-cloud connected layer below cloud layer* (Figure 1b2), where the overlying cloud can be multiple layers. *Aerosol-cloud connected layer above cloud layer* is the

third group of the connected-cloud aerosol (Figure 1b3), where the underlying cloud can be multiple layers. All the connected-cloud aerosol profiles not beyond to the first three groups will be included in the four subcategories (*other connected-cloud* aerosol), including the profiles with more than one aerosol-cloud connected layers, or multi-layer aerosols or/and multi-layer clouds with at least one aerosol-cloud connected layer. Figure 1d4 gives an example of the *other connected-cloud* aerosol profile. The *isolated-cloud* aerosol is grouped in a similar way. The below-cloud (Figure 1c1) aerosol can have multiple layers for the overlying clouds or the underlying aerosols. Similarly, the above-cloud aerosol (Figure 1c2) can also contain multi-layer underlying clouds or multi-layer overlying aerosols. Any profiles of the isolated-cloud aerosols that don't beyond to the first two subgroups will be grouped as other isolated-cloud aerosols. Figure 1c3 gives an example.

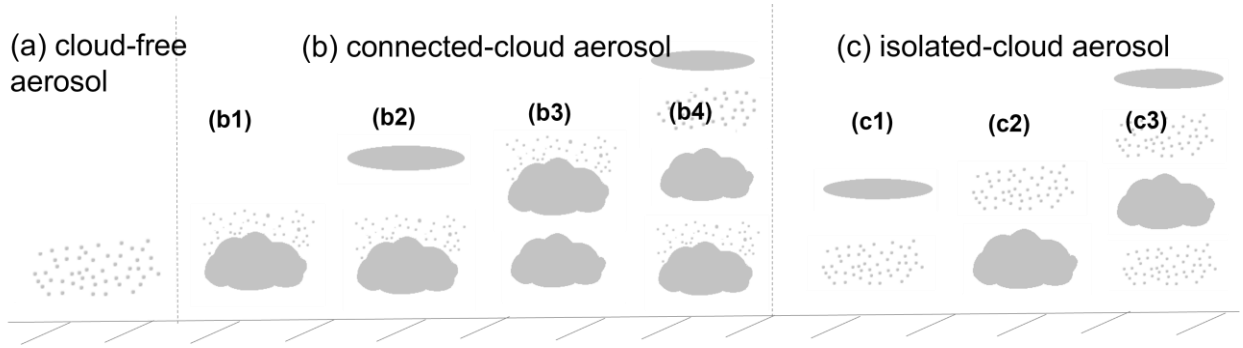

Figure 1. Aerosol scenarios in clear sky (a) and cloudy sky (b-c). (b) Aerosols in the column where there are at least one aerosol and cloud layer vertically connected (connected-cloud aerosol): (b1) only one aerosol and one cloud layer in the column but vertically connected (one-layer aerosol-cloud connected), (b2) the aerosol-cloud connected layer below cloud layer, (b3) the aerosol-cloud connected layer above cloud layer, and (b4) an example for multi-layer aerosol or/and multi-layer cloud that doesn't beyond to (b1-b3) (other connected-cloud aerosol). (c) Aerosols in the column where there are no aerosol and cloud layers vertically connected: (c1) below-cloud aerosol, (c2) above-cloud aerosol, and (c3) an example for multi-layer aerosol or/and multi-layer cloud that doesn't beyond to (c1-c2) (other isolated-cloud aerosol).

Figure 2 shows a CALIPSO curtain applied our aerosol classification method as described in Section 2.3. The shape in red indicates aerosol, while in blue indicates cloud. One can clearly see the below-cloud aerosol in the regions marked by the red dots at 20 km, the above-cloud aerosol indicated by the pink dots, and the group of the one-layer aerosol-cloud connected aerosols in green.

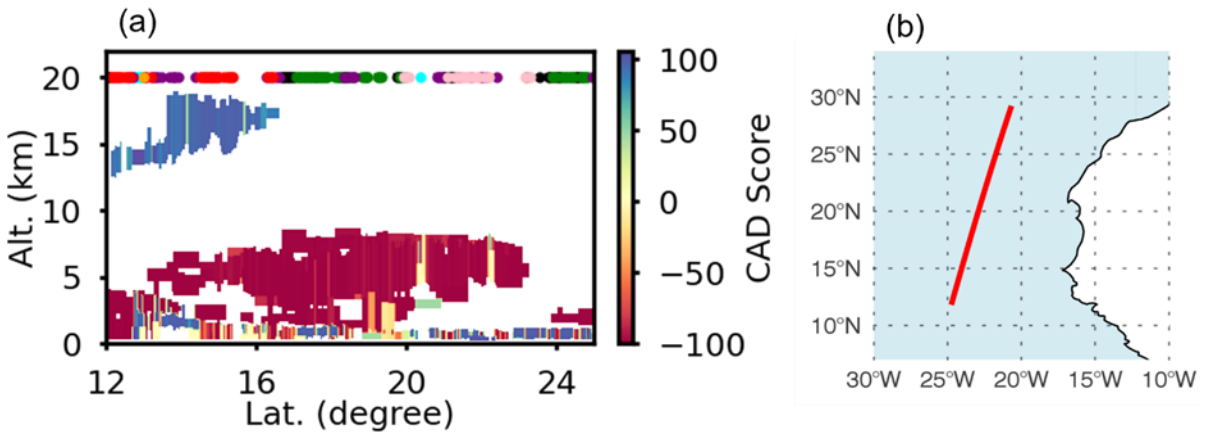

Figure 2. (a) Cloud-aerosol groups for a case on Jul. 24th, 2019 when CALIPSO overpassed above the Atlantic Ocean as shown in (b). The filled circles marked at 20 km flag the aerosol classification as in Figure 1: black for the cloud-free, green for the one-layer aerosol-cloud connected, blue for the aerosol-cloud connected layer below cloud layer, cyan for the aerosol-cloud connected layer above cloud layer, purple for the other connected-cloud aerosol; red for the below-cloud aerosol, pink for the above-cloud aerosols, and orange for the other isolated-cloud aerosol.

3. Results and Discussion

3.1 Global Distributions of The Cloud-free and The Cloudy Aerosols

Figure 3 shows the global distributions of aerosol fraction (AF or f_a) in clear (Figure 3a) and cloudy (Figure 3b) skies. Aerosol fraction (Equation 1) is defined as the samples of one aerosol group such as the cloud-free or the cloudy aerosols, divided by all samples with $\tau_a > 0$ that pass the quality filters as discussed in Section 2.2. As expected, the global distributions of the cloud-free and the cloudy aerosols detected by CALIOP follow the climatology of clear and cloudy skies. Specifically, in the subtropical regions, the cloud-free aerosols are dominated with f_a higher than 60%. For the cloudy aerosols, they widely spread in the tropical regions where associate with ubiquitous cirrus clouds (Hong & Liu, 2015; Sassen et al., 2008) and in the subtropics such as west of South Africa where stratocumulus deck is prevailing (Sassen & Wang, 2008). As a result, negative f_a difference (cloudy – cloud-free) is observed over most of the subtropical regions and positive f_a difference occurs over the tropics (Figures 3e and 3g).

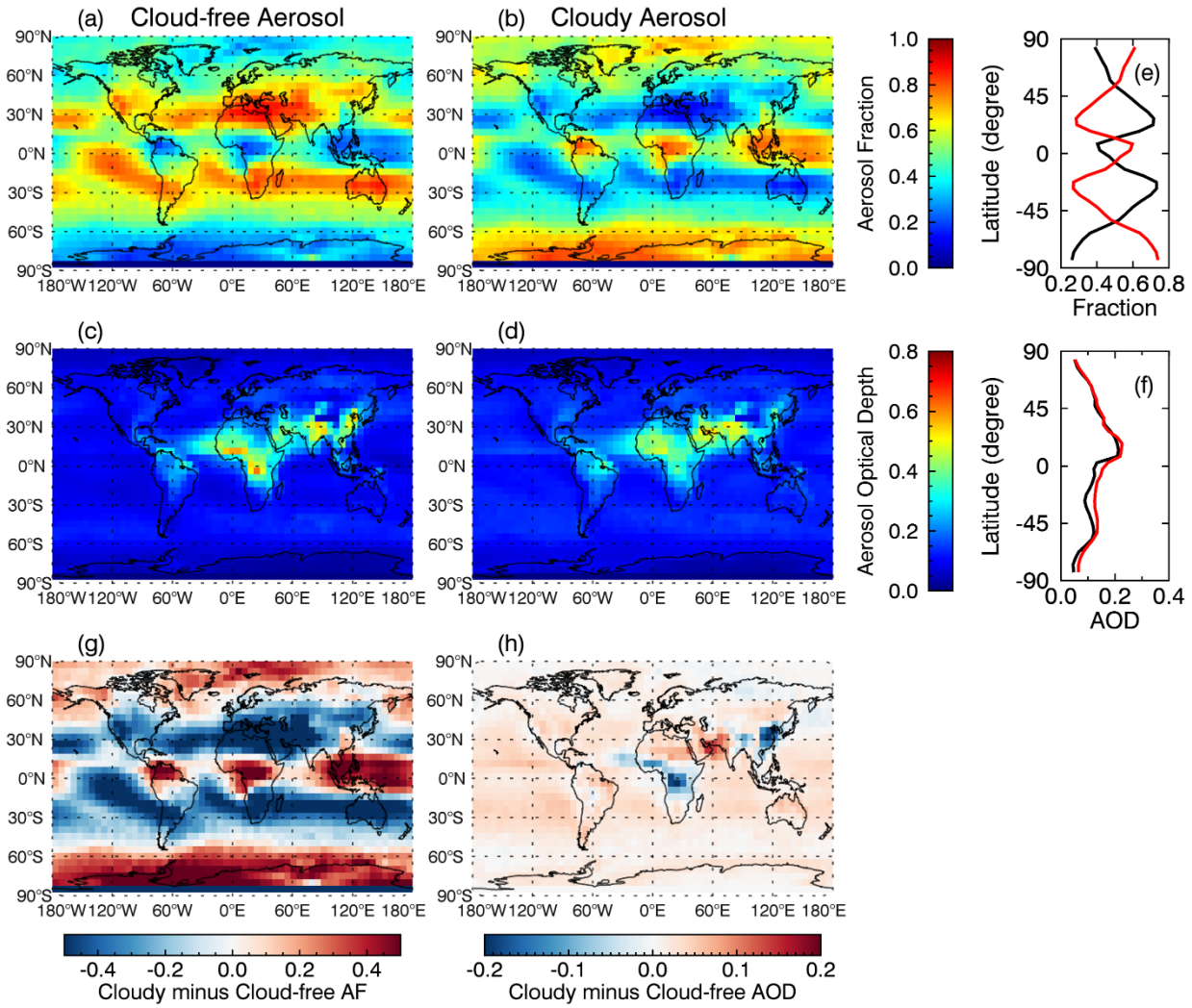

Figure 3. Global distributions of aerosol fraction and optical depth in cloud-free and cloudy skies shown in (a)-(d). Zonal averages of aerosol fraction (e) and optical depth (f): black for the cloud-free aerosol and red for the cloudy aerosols. (g) and (h) are for the aerosol fraction and optical depth differences between the cloudy and the cloud-free aerosols.

Mean AOD in each 6° long by 5° lat grid is calculated as the summation of optical depth divided by the total sample with $\tau_a > 0$ for each aerosol group. As shown in Figures. 3c and 3d, both the cloud-free and the cloudy aerosols display relatively large values (e.g. $\tau_a > 0.4$) over Africa, Center Atlantic Ocean, Arabian and Indian Peninsula, and East Asia. We also observe some large τ_a values (~ 0.2) over the trade wind (easterly, such as Pacific ocean) and midlatitude storm track (westerly) regions than the nearby ocean, corresponding to the sea-salt aerosols (Grythe et al., 2014). This pattern is consistent with the aerosol climatology derived from MODIS (Remer et al., 2008). The cloudy τ_a is generally higher over the globe, especially over Arabian Sea and its surrounding regions, whereas over the Southeast Asia and Center Africa, cloud-free τ_a is larger (Figure 3h).

Over the globe, aerosols detected by CALIOP have about 55.9% samples occurring in clear sky, and another 44.1% occurring in cloudy sky. Cloudy aerosols occupy a smaller

proportion because aerosols with low concentrations or under opaque clouds undergo undetected by CALIOP.

The global mean aerosol optical depth ($\bar{\tau}_a$), calculated as Equation (2), and the global mean $\tau_a$uncertainty for clear sky are about 0.135±0.047, while in cloudy sky, they are about 0.143±0.074. For all aerosols, $\bar{\tau}_a$ is about 0.139±0.059. An averaged AOD difference of 0.08 between the cloudy and cloud-free aerosols is significant based on t-test analysis. The uncertainty of the cloudy-sky aerosol is much larger than the cloud-free aerosol, indicating bigger challenge to retrieve aerosols in cloudy sky (Winker et al., 2009).

$$f_{ai} = n_{ai}/N_{ai} \quad (1)$$
$$\bar{\tau}_a = \sum_i \tau_{ai} n_{ai} / \sum_i n_{ai} \quad (2)$$

where i represents the i[th] grid, n_{ai} and N_{ai} are the samples for one aerosol group and total aerosol samples with quality control in that grid.

Figure 4 displays the profiles of aerosol samples and lidar backscatter (β) for cloud-free (black) and cloudy (red) skies globally. As displayed, aerosols are mostly detected in the boundary layer (< 2 km) with a peak occurrence at ~ 1 km, and evident aerosols are also observed between 2 - 4 km. The average lidar backscatter profiles (solid lines in Figure 4b) show that the cloudy aerosols have stronger backscatter along all altitudes than the cloud-free aerosols. Yet the median lidar backscatter profiles show slightly stronger backscatter for the cloudy aerosols only under the boundary layer. Above the boundary layer, the median lidar backscatters are quite consistent between the cloudy and the cloud-free aerosols. Larger lidar backscatter in cloudy sky agrees with larger cloudy τ_a.

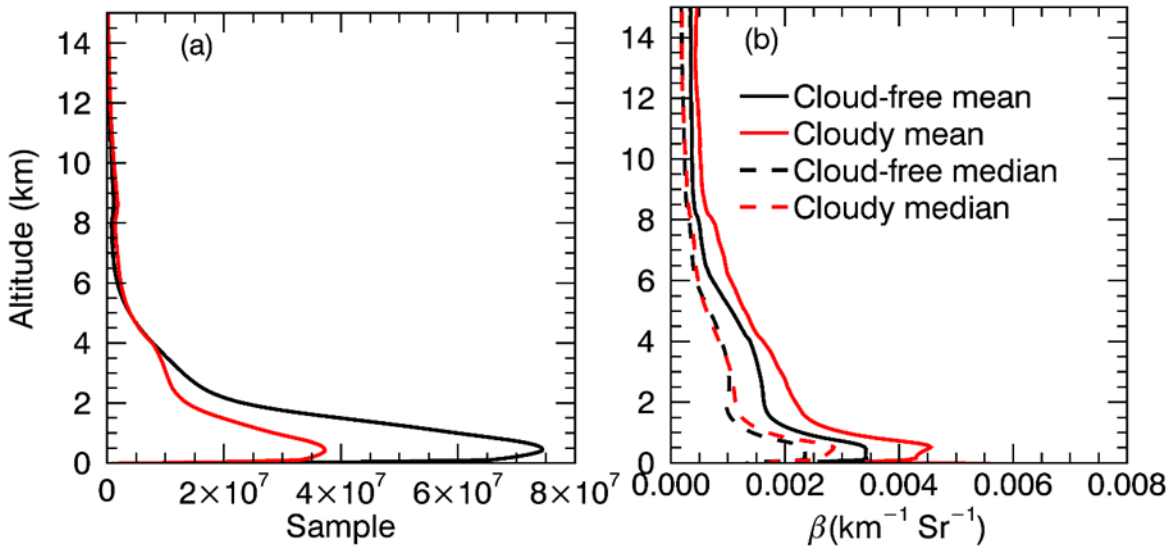

Figure 4. Number of samples (a) and lidar backscatter profiles (b): red for the cloudy aerosol, black for the cloud-free aerosol, solid line for mean values and dashed line for median values. The vertical resolution is same as Level-2 aerosol profile data, i.e. 30 m below 8.2 km and 60 m above 8.2 km.

3.2 Global Distributions of The Connected-cloud and The Isolated-cloud Aerosols

To investigate the detailed characteristics of aerosols in cloudy sky, Figures 5 and 6 display the global distributions of f_a and τ_a for the connected-cloud and the isolated-cloud aerosols.

As showed, the connected-cloud aerosols are mainly occupied by the one-layer aerosol-cloud connected and the aerosol-cloud connected layer below cloud layer groups, which account for about 8.8% and 3.4% among all aerosols detected by CALIOP, respectively (Figures 5a1 and 5a2). For the one-layer aerosol-cloud connected aerosols, relatively large f_a primarily occurs over the west of continents where marine stratocumulus are prevailing, including Center and North Atlantic where are polluted by the westward transferred Sahara dust (Devasthale & Thomas, 2011; Yang et al., 2012; Zhang et al., 2016), Southeast Atlantic where biomass burning smoke is advected from South Africa during the local winter/spring seasons (Devasthale & Thomas, 2011; Zhang et al., 2016), as well as West of North and South America, and West of Australia. Also, the one-layer aerosol-cloud connected aerosols are frequent over East Asia where low-level stratocumulus are prevailing during spring and winter (Hong & Di Girolamo, 2020; Klein & Hartmann, 1993), providing high change for clouds embedding to aerosol layers in the lower troposphere. For the aerosol-cloud connected layer below cloud layer group, they primarily distribute over the tropics and midlatitude storm tracks where cirrus clouds are prevailing (Hong & Liu, 2015; Sassen et al., 2008). The aerosol-cloud connected layer above cloud layer and other connected-cloud aerosols account for about 1.6% and 2.9%, respectively, among all detected aerosols.

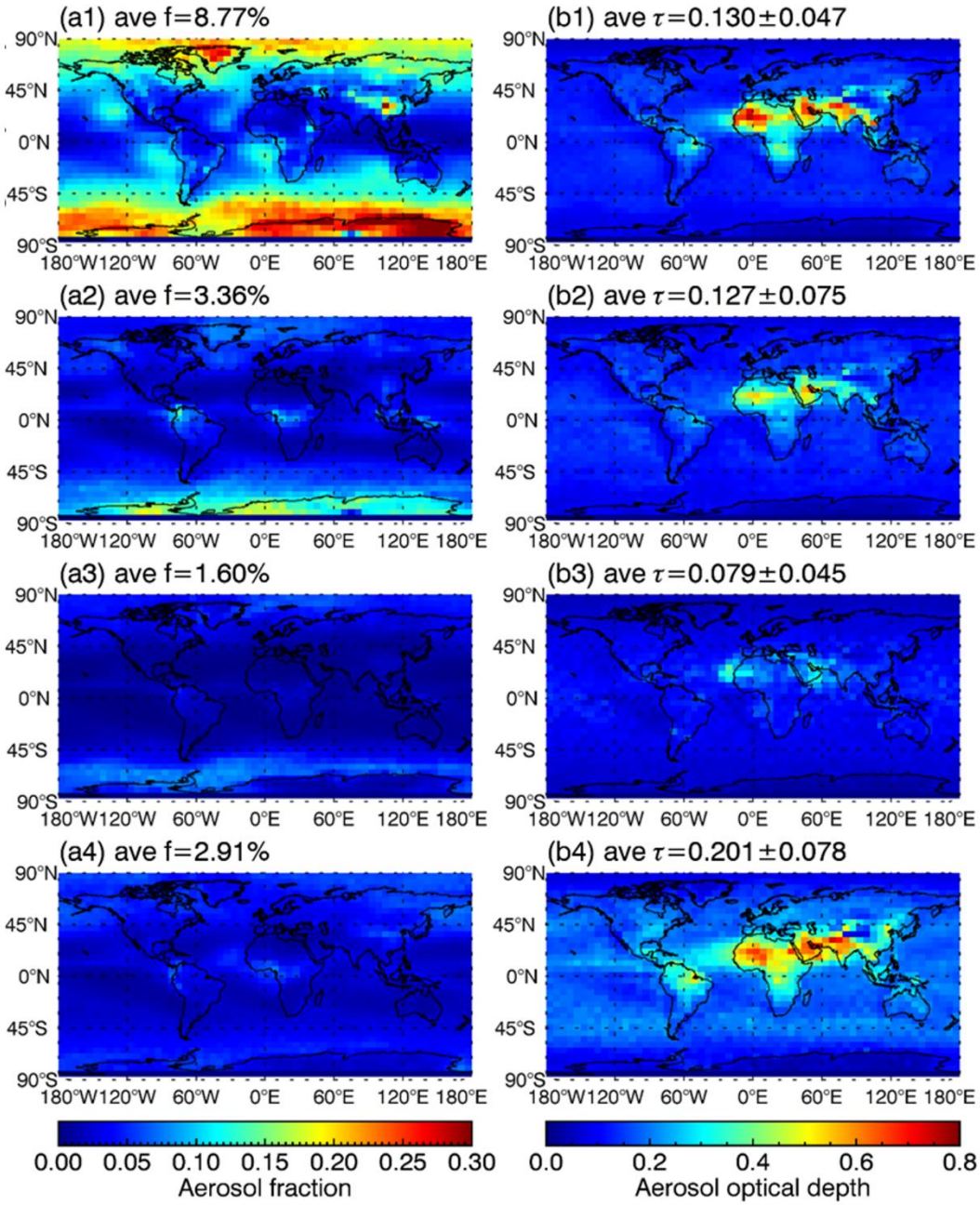

Figure 5. Aerosol fraction (a1-a4) and optical depth (b1-b4) for the four subgroups of the connected-cloud aerosol: first row for the one-layer aerosol-cloud connected, second row for the aerosol-cloud connected layer below cloud layer, the third row for the aerosol-cloud connected layer above cloud layer, and the bottom row for the other connected-cloud aerosol.

For optical depth, the one-layer aerosol-cloud connected (Figure 5b1) and the aerosol-cloud connected layer below cloud layer aerosols (Figure 5b2) show similar spatial patterns with the cloud-free aerosols but their global means are smaller. The aerosol group of the aerosol-cloud connected layer above cloud layer has the smallest mean τ_a (Figure 5b3), while the other connected-cloud aerosols have the largest τ_a, particularly over ocean and over the 'dust belt' cross Sahara eastward to Arabia and Southwest of Asia (Figure 5b4). Also, the aerosol-cloud

connected layer below cloud layer (Figure 5b2) and the other connected-cloud aerosols (Figure 5b4) have larger τ_a uncertainties than the other two connected-cloud aerosol groups, i.e. the one-layer aerosol-cloud connected (Figure 5b1) and the aerosol-cloud connected layer above cloud layer (Figure 5b3). The overlying clouds induce additional uncertainty to the lower aerosol layers as discussed in Section 1 (Winker et al., 2009).

Figure 6 shows the distributions of the isolated-cloud aerosols. The below-cloud aerosols (Figure 6a1) account for about 21.2% among all aerosols, frequently distributing in the tropical regions where occur ubiquitous cirrus clouds (Hong & Liu, 2015; Sassen et al., 2008). The fraction of the above-cloud aerosols (Figure 6a2) are about 4%, and are primarily distributed over ocean, i.e. West of the Africa and America continents, as well as East of Asia continent, agreeing with the results from previous research that focused on the above-cloud aerosols (Devasthale & Thomas, 2011; Yang et al., 2012; Zhang et al., 2016). For the other isolated-cloud aerosols (Figure 6a3), their global average fraction is about 2%. The $\bar{\tau}_a$~ 0.165 of the below-cloud aerosols is larger than that of the cloud-free aerosols ($\bar{\tau}_a \sim 0.135$). The above-cloud aerosols have smaller $\bar{\tau}_a$ (0.056) than the cloud-free aerosols primarily due to a shallower integrated column than the cloud-free aerosols. Also, aerosol optical depth uncertainties of the below-cloud and other isolated-cloud groups tend to be larger than the cloud-free or the above-cloud aerosols. The retrieved cloud attenuation used for the underlying layer signal correction responds for the additional uncertainty to aerosol layers (Chung et al., 2016; Winker et al., 2009).

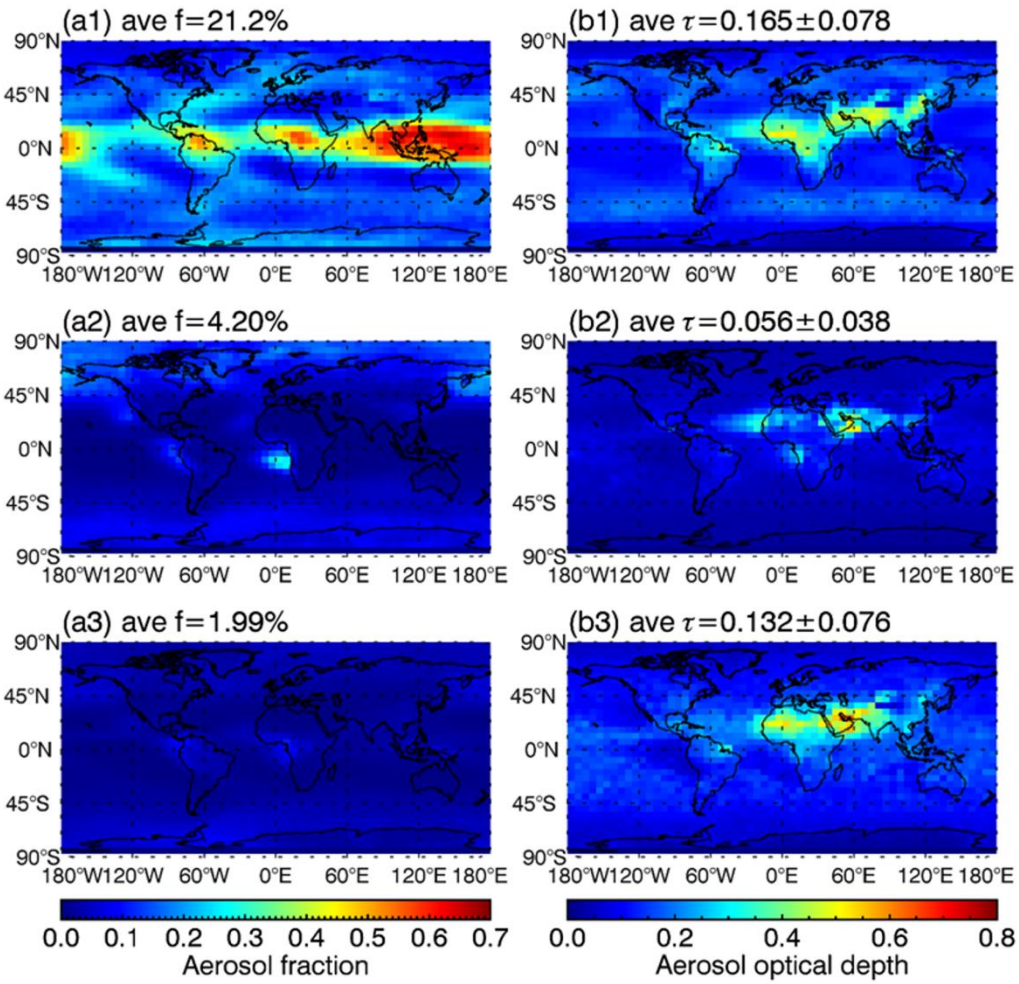

Figure 6. Same as Figure 5 but for the isolated-cloud aerosol: the upper panels for below-cloud aerosol, the middle panels for above-cloud aerosol, and the lower panels for the other isolated-cloud aerosol.

It has been noted that the cloudy aerosols are primarily occupied by the below-cloud aerosols (f_a ~ 21%), which account for almost half of the detected cloudy aerosols (f_a ~ 44%). Considering that aerosols under opaque clouds are missed by CALIOP, the below-cloud aerosols are more spread than what we observe from Figure 6a1. Liao and Seinfeld, (1998) stated that a cirrus cloud layer causes modest changes of aerosol radiative effect at TOA, which is about 1 W m^{-2} change compared to no cirrus presence in their radiative transfer simulations. The wide coverage of the below-cloud aerosols indicates that the impact of cirrus to aerosol direct radiative effect could be significant over the globe.

It is also noted that the τ_a uncertainties are larger for those aerosols with overlying cloud layers in the column, i.e. the aerosol-cloud connected layer below cloud layer and below-cloud aerosols, compared to the situations without overlying cloud presence, i.e. the one-layer aerosol-cloud connected and the cloud-free aerosols. In Section 3.3, we further check more details of τ_a distributions and other aerosol properties to investigate whether there is any similarity between aerosols with and without overlying cloud layers.

3.3 Optical Property and Lidar Variables

3.3.1 Optical Depth

The probability density functions (PDF) of τ_a are shown in Figure 7 for the cloud-free, the connected-cloud and the isolated-cloud aerosols. The cloud-free τ_a PDF is nearly a lognormal distribution with a peak at $\tau_a \sim 0.083$ (Table 3). For the connected-cloud aerosols, their PDFs are generally fatter than the cloud-free aerosols and have higher frequencies at small τ_a regions. The one-layer aerosol-cloud connected and the aerosol-cloud connected layer below cloud layer aerosols show close PDFs (Figure 7a, pink and red), close values in their means, modes and medians (Table 3, b1 and b2) with a comparison with other aerosol groups. The PDF of the aerosol-cloud connected layer above cloud layer aerosols (Figure 7a, green) shows much higher frequency when $\tau_a < \sim 0.04$ with the smallest median, mode and median values among all the connected-cloud aerosol groups.

Similarly, for the isolated-cloud aerosols, the below-cloud aerosols show a very close PDF with the cloud-free aerosols but with slightly larger mode (~ 0.089), median and mean values (Table 3, c1). In contrast, the above-cloud aerosols have much smaller mode values than the cloud-clear aerosols as shallower aerosol columns contribute to a smaller τ_a.

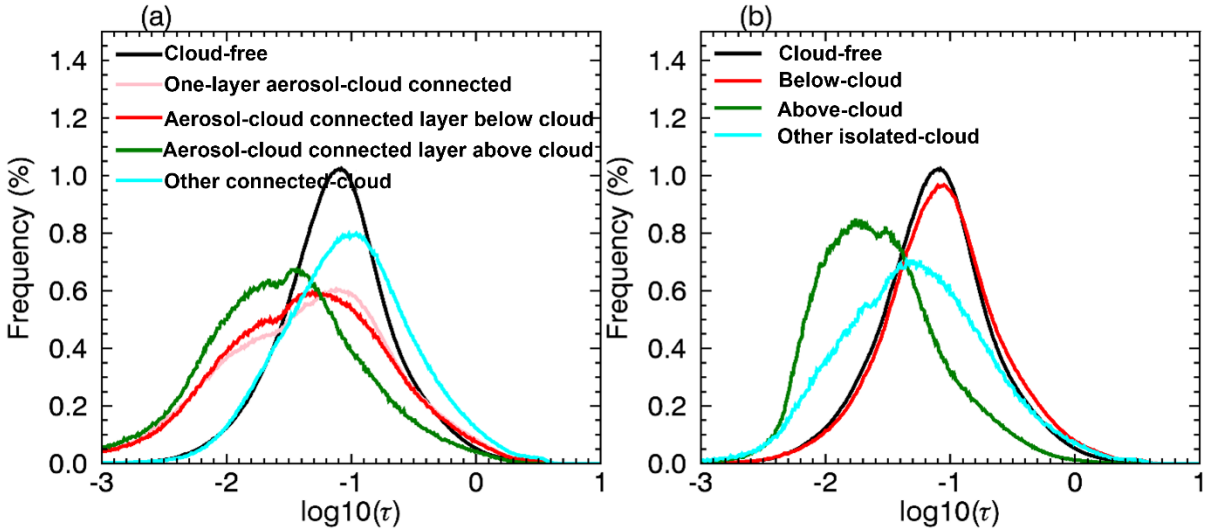

Figure 7. The probability distribution functions of AOD for global aerosols: (a) the connected-cloud aerosols and (b) the isolated-cloud aerosols with a contrast to the cloud-free aerosols shown in black curve in both (a) and (b).

Table 3 The AOD medians, modes and means for the cloud-free, the connected-cloud and the isolated-cloud aerosols. b1-b4 and c1-c4 represent the same aerosol categories as Figures 1b1-b4 and Figures c1-c4, respectively.

	Cloud-free	Connected-cloud				Isolated-cloud		
		b1	b2	b3	b4	c1	c2	c3
Median	0.076	0.048	0.043	0.027	0.093	0.083	0.024	0.050
Mode	0.083	0.075	0.052	0.038	0.110	0.089	0.017	0.048
Mean	0.135	0.130	0.127	0.079	0.201	0.165	0.056	0.132

3.3.2 Depolarization Ratio and Lidar Backscatter

The integrated attenuated backscatter and depolarization ratio (δ) are two important variables for constraining aerosol type selections (Omar et al., 2009). Figure 8 shows the two-dimensional (2-D) histogram of β versus δ for the detected aerosol layers. As displayed, most of the one-layer aerosol-cloud connected (Figure 8a), the aerosol-cloud connected layer below cloud layer (Figure 8c), the cloud-free (Figure 8b), and the below-cloud aerosols (Figure 8d) have $\delta < 0.02$. In contrast, the aerosol-cloud connected layer above cloud layer (Figure 8e) and the above-cloud aerosols (Figure 8f) show tremendous samples with $\delta > 0.02$. These two groups of aerosols distribute in the regions where are frequently affected by dust and biomass burning (Figures 5a3 and 6a2), being consistent with that relatively large δ indicates desert dust and biomass burning aerosols (Burton et al., 2012; Omar et al., 2009). Moreover, the connected-cloud aerosols tend to have lidar backscatter (β) less than $0.001\ \mathrm{Sr}^{-1}km^{-1}$, agreeing with higher frequency at small τ_a region in Figure 7a. For the cloud-free and the below-cloud aerosols, they have most samples with $\beta > 0.001\ \mathrm{Sr}^{-1}km^{-1}$, indicating marine and polluted continental aerosols (Omar et al., 2009). The above-cloud aerosols rarely have $\beta > 0.001\ \mathrm{Sr}^{-1}km^{-1}$. Again, the cloud-free and the below-cloud aerosols share similar $\beta - \delta$ diagram with the samples concentrated in the regions of $\beta > 0.001\ \mathrm{Sr}^{-1}km^{-1}$ and $\delta < 0.02$. It is also similar for the one-layer aerosol-cloud connected and the aerosol-cloud connected layer below cloud layer aerosols who have a similar pattern of $\beta - \delta$ diagram with the samples concentrated in two regions: 1. $\beta \sim 0.0003 - 0.001\ \mathrm{Sr}^{-1}km^{-1}$ and $\delta < 0.02$ and 2. $\beta \sim 0.003\ \mathrm{Sr}^{-1}km^{-1}$ and $\delta < 0.02$.

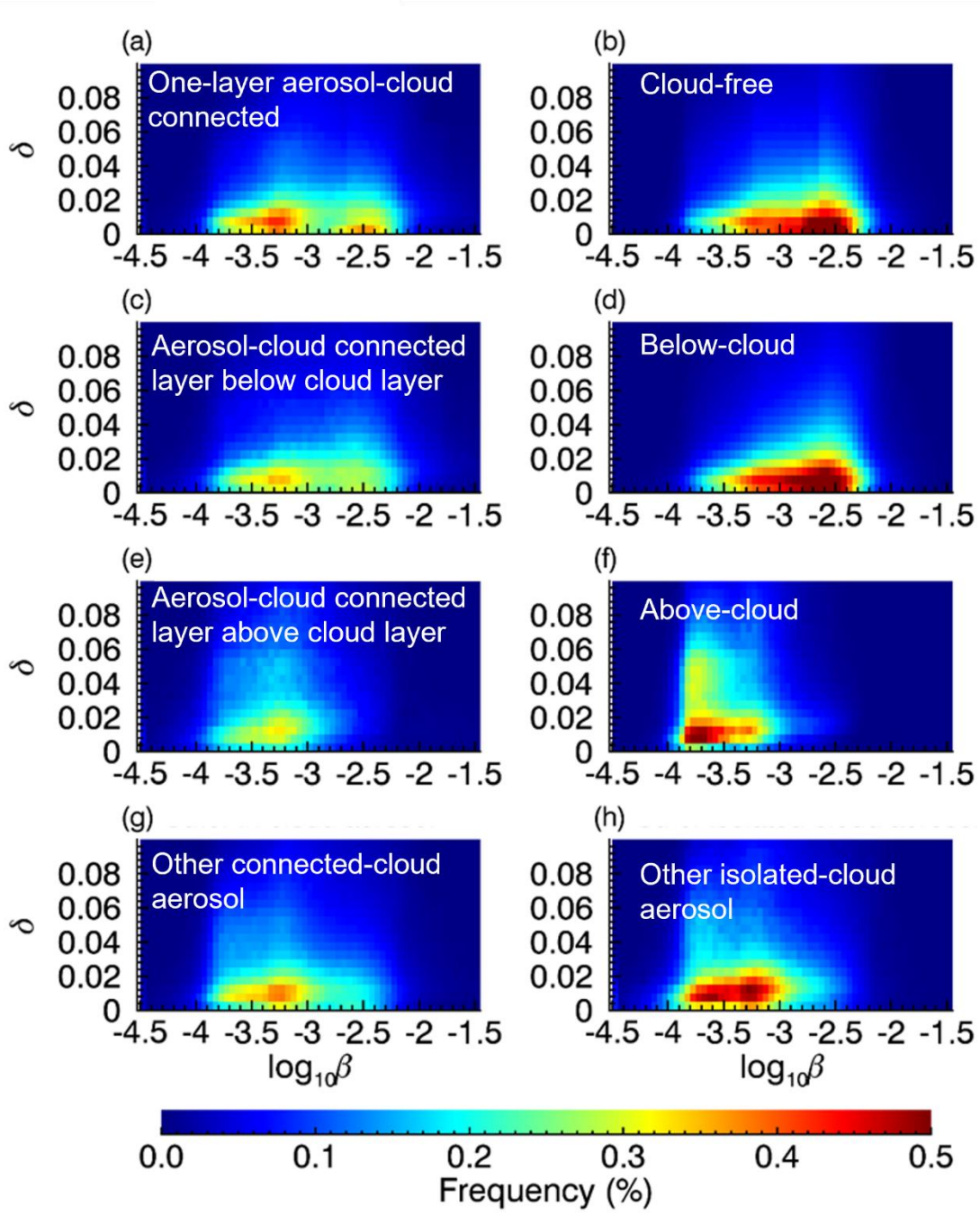

Figure 8. Two-dimensional histogram of lidar backscatter (in $\log_{10}$ scale) vs. depolarization ratio for the cloud-free, the connected-cloud and the isolated-cloud aerosols. The total frequency of each diagram is equal to 100.

3.3.3 Lidar Ratio and Color Ratio

Lidar ratio (Sr), i.e. the extinction coefficient to lidar backscatter ratio, is essential to obtain optical depth. The CALIPSO aerosol type classification assigns one Sr to one aerosol type (Omar et al., 2009). In the V4 data, lidar ratio has been updated to better represent aerosol types

(Kim et al., 2018). Six main aerosol types are manifested in Figure 9, i.e.: clean marine ($\mathrm{Sr} = 23$), dusty marine ($\mathrm{S} = 37$), dust/volcanic ash ($\mathrm{Sr} = 44$), clean continental ($\mathrm{Sr} = 53$), polluted dust ($\mathrm{Sr} = 55$) and polluted continental/smoke/elevated smoke (Sr = 70) aerosol. The dots and error bars in Figure 9 represent means and standard deviations of color ratio (γ) for each aerosol type. The number near each aerosol type is obtained by integrating the frequency over y axis, i.e. color ratio, representing the proportion of each aerosol type within that aerosol group. For instance, Figure 9b shows that the cloud-free aerosols contain about 45.9% samples being classified as clean marine aerosols.

The proportions of aerosol types in each aerosol group are closely related to aerosol distributions over the globe. Clean marine aerosols are the primary aerosol type for the cloud-free (Figure 9b, 45.9%), the one-layer aerosol-cloud connected (Figure 9a, 36.5%), the aerosol-cloud connected layer below cloud layer (Figure 9c, 32.5%) and the below-cloud (Figure 9d, 49.8%) aerosols. In particular, the below-cloud aerosols show a similar $Sr - \gamma$ pattern with the cloud-free aerosols. The cloud-free aerosol group is slightly larger in the proportions of dust/volcanic ash and polluted dust aerosols, while the below-cloud aerosol group is about 4% and 1.3% higher in clean marine and dusty marine aerosols. For the above-cloud (Figure 9f) and the aerosol-cloud connected layer above cloud layer aerosols (Figure 9e), they share similar aerosol types as well. Dust/volcanic ash (> 30%), polluted dust (~ 24%) and elevated smoke (~ 25%) are the three dominated aerosol types, but the clean marine or dusty marine aerosols are rare (< 5%) for these two aerosol groups. The mean and standard deviation of color ratio between the cloud-free and the below-cloud aerosols are similar with the mean color ratio of about 0.5 for clean marine, dusty marine and dust/volcanic ash aerosols, about 0.4 for polluted dust and polluted continental/smoke/elevated smoke, and about 0.2 for clean continental aerosols.

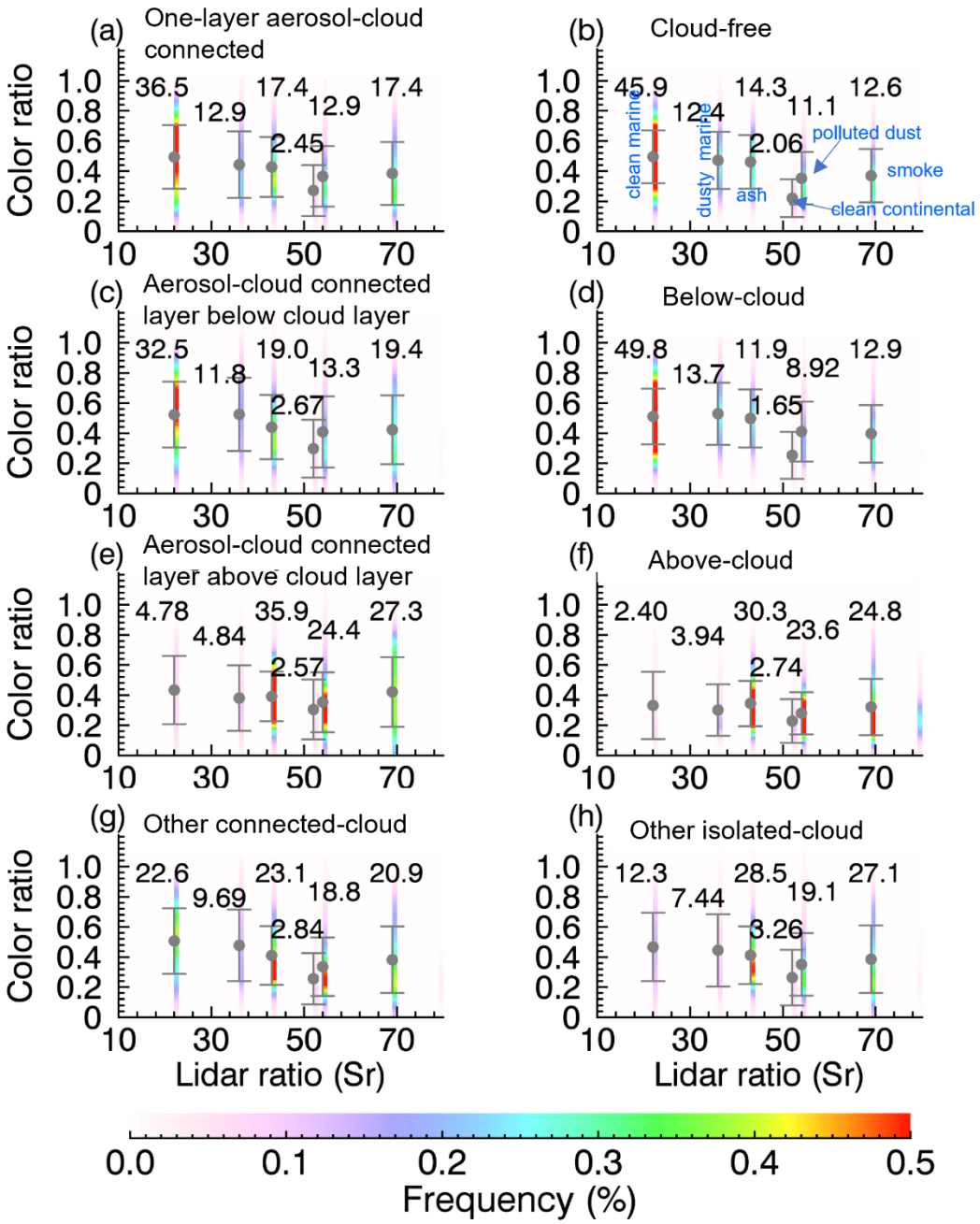

Figure 9. 2-D histograms of lidar ratio vs. color ratio. The gray dots and error bars represent the mean and standard deviation of color ratio, while the number represents the total fraction of each aerosol type.

Overall, the τ_a distributions, the $Sr-\gamma$ and $\beta-\delta$ diagrams have shown similarity between the one-layer aerosol-cloud connected and the aerosol-cloud connected layer below cloud layer aerosols as well as between the cloud-free and the below-cloud aerosols. Some differences in these properties between aerosols with and without overlying clouds could result from their contrast in spatial distributions as discussed in Section 3.2, from the accuracy of

cloud-aerosol discrimination, from additional uncertainties induced by the overlying cloud layers as well as from a modification of aerosol properties by cloud layers.

3.4 Regional and Seasonal Analysis

As displayed in Section 3.2, aerosols unevenly distribute over the globe. To characterize the regional aerosol variability, we show aerosol properties in cloudy and clear skies for nine selected locations as indicated in Figure 10 where are significantly affected by anthropogenic and natural activities. Figures 11 and 12 display the timeseries of monthly $\bar{f}_a$ and $\bar{\tau}_a$ for the cloud-free (red), the cloudy (orange, a combination of the connected-cloud and the isolated-cloud), the connected-cloud (green), the isolated-cloud (grey) aerosols. Figures 13 and 14 show the profiles of aerosol samples and median lidar backscatters.

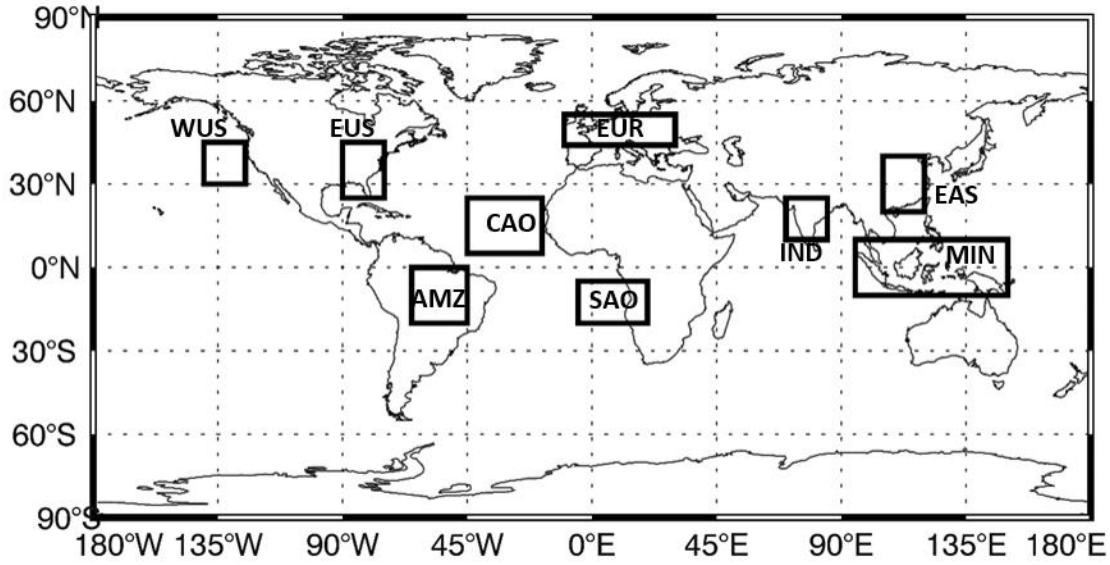

Figure 10. Selected areas for studying the seasonal variations of aerosol fraction and optical depth derived from CALIOP: EAS short for East Asian region, MIN for Malaysian-Indonesia region, IND for Indian region, EUR for European region, CAO for Center Atlantic Ocean, SAO for Southeast Atlantic Ocean, EUS for East US, WUS for west of US, AMZ for Amazonian region.

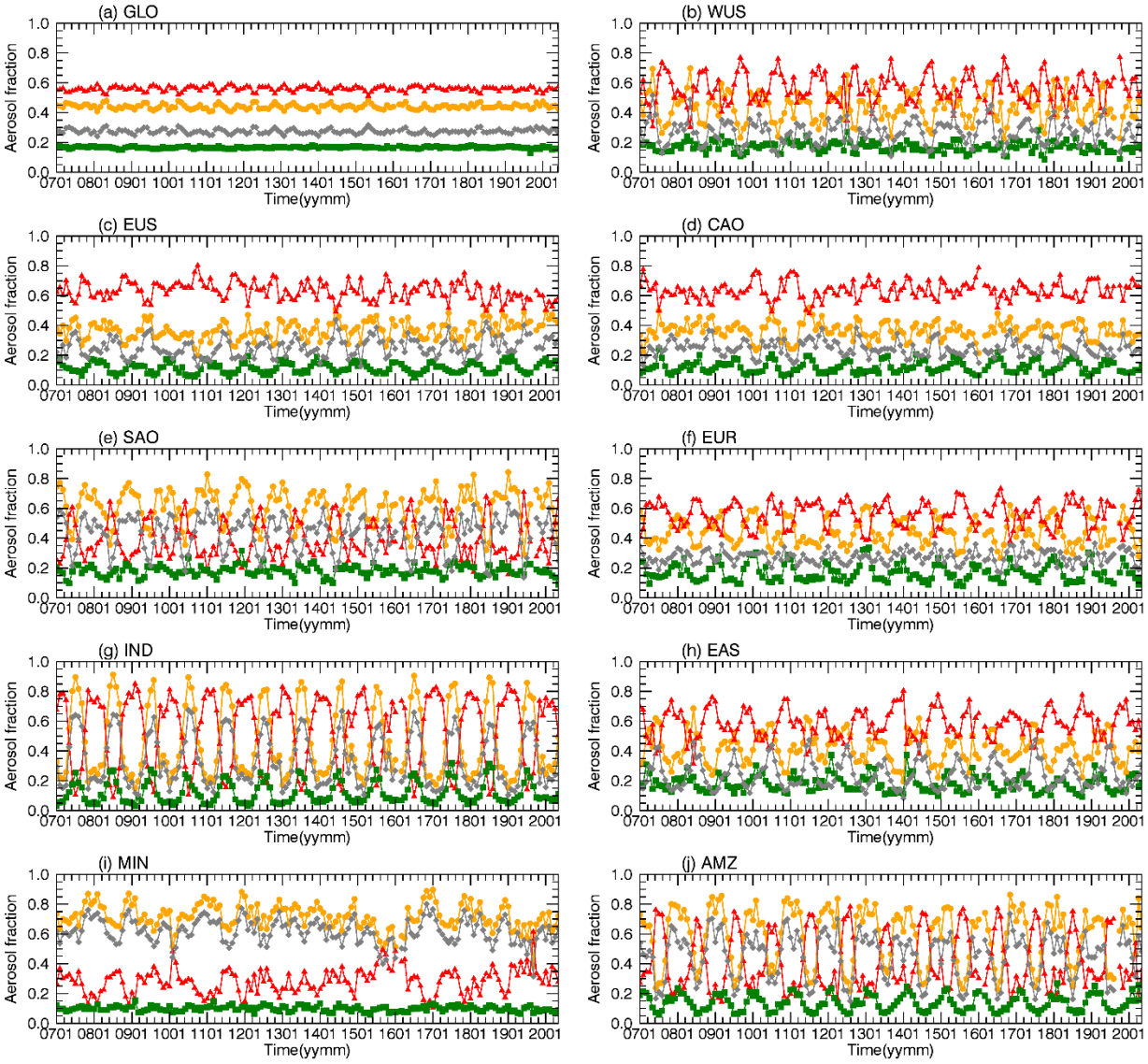

Figure 11. The timeseries of aerosol fraction for the selected regions as displayed in Figure 10: red- the cloud-free aerosol, orange – the cloudy aerosol, green – the connected-cloud aerosol, grey- the isolated-cloud aerosol.

For the whole globe, the cloudy and the cloud-free $\bar{\tau}_a$ values show seasonal variations ranging roughly from 0.1 to 0.15, being larger during boreal summer and smaller during boreal winter (Figure 12a). The seasonal variations agree with results from passive sensor measurements such as MODIS and MISR (Mehta et al., 2016; Mishchenko et al., 2007; Remer et al., 2008). In contrast, the cloud-free and cloudy aerosol fractions are quite flat (Figure 11a).

In different regions, the variations of $\bar{\tau}_a$ and $\bar{f}_a$ differ significantly between the cloud-free and the cloudy aerosols which rely on the variations of cloud systems, local emissions, and long-track transport. For example, in the Malaysia-Indonesia regions (Figures 11-14i), the fraction of aerosols in cloudy sky, primarily contributed by the below-cloud aerosols (Figure 6a), is twice more than that of the cloud-free aerosols due to the ubiquitous cirrus in this region (Figure 11i). The cloudy $\bar{\tau}_a$ is slightly larger than the cloud-free $\bar{\tau}_a$, while the connected-cloud $\bar{\tau}_a$ is the

largest in this region (Figure 12i). The climate impact in this region is observable – the cloud-free aerosols account for a higher fraction during the winter-spring seasons of 2009-2010, 2015-2016 and 2019-2020 when El Niño phase dominated; during the La Niña years such as 2010, 2017 and 2018, cloudy aerosols have larger fractions. The detected aerosols primarily occur below 4 km (Figure 13i). The median backscatter profiles (Figure 14i) also display that the connected-cloud aerosols tend to have the largest backscatter, extending up to 4 km. The isolated-cloud and the cloud-free aerosols have their median backscatter profiles nearly overlapped below 4 km, indicating the similarity between aerosols with and without clouds overlying.

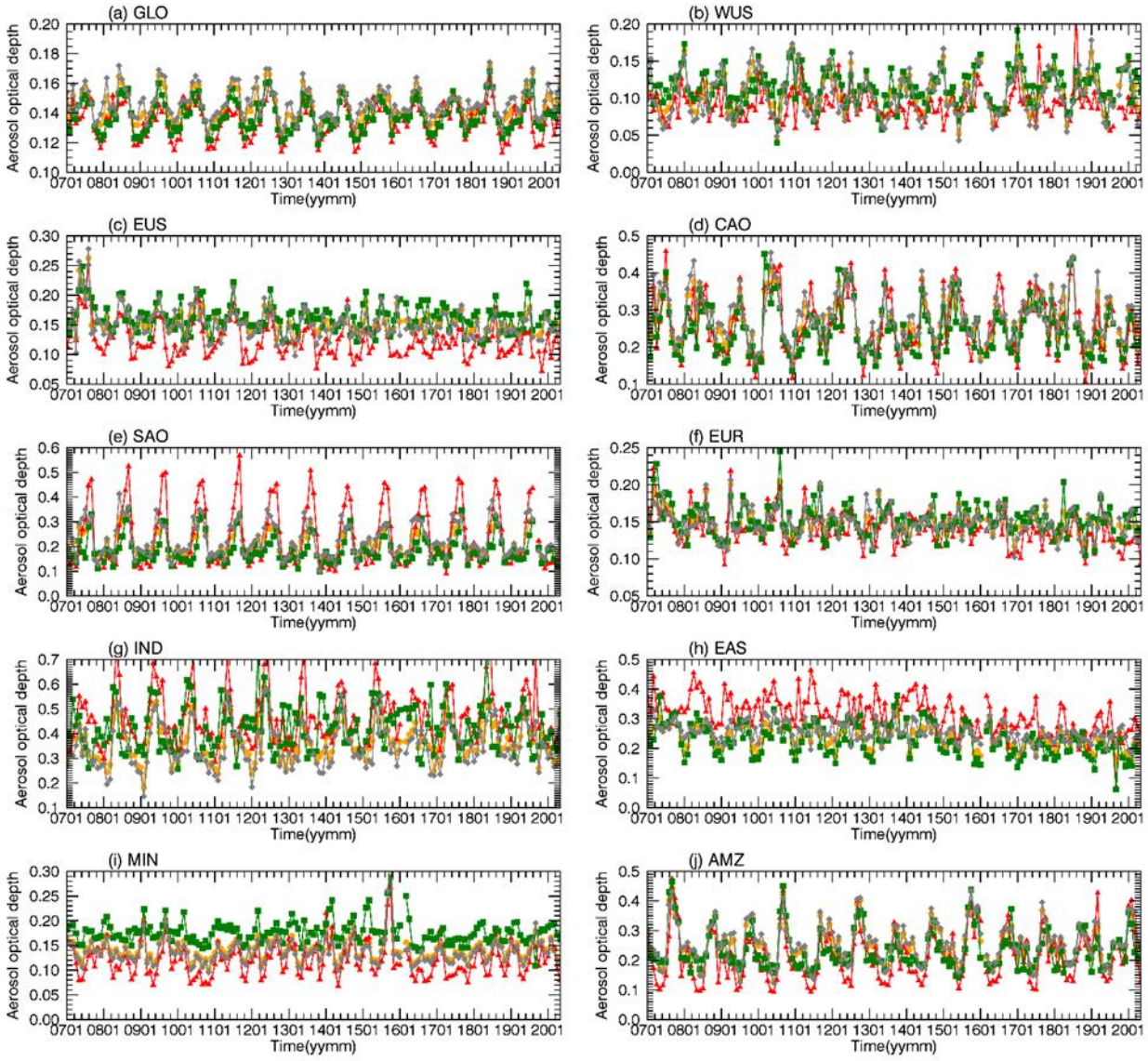

Figure 12. Same as Figure 11 but for the timeseries of aerosol optical depth.

In the Southeast Atlantic region, aerosols frequently transport above stratocumulus during the biomass burning season (local winter) (Zhang et al., 2016) when the cloud-free aerosols account for almost 60% among all detected aerosols (Figure 11e). The cloudy aerosols up to 80% during local summer are primarily contributed by the isolated-cloud (above-cloud)

aerosols. The cloud-free aerosols show that $\bar{f}_a$ peaks in May-Aug. $\bar{\tau}_a$ in this region is larger in local winter and smaller during summer (Figure 12e). The connected-cloud and the isolated-cloud τ_a are smaller than the cloud-free aerosols in this region because aerosols are frequently transferred above stratocumulus so that cloudy τ_a is being integrated in a shallower column than in clear sky. This is also revealed in Figure 13e that shows a peak located at ~ 3 km, i.e. above boundary layer, and another peak in boundary layer (~ 1 km). It is obvious that there are two bumps in the median backscatter profiles (Figure 14e) - one below 1 km and another one between 2-6 km, contributing by the boundary-layer and the elevated aerosols, respectively.

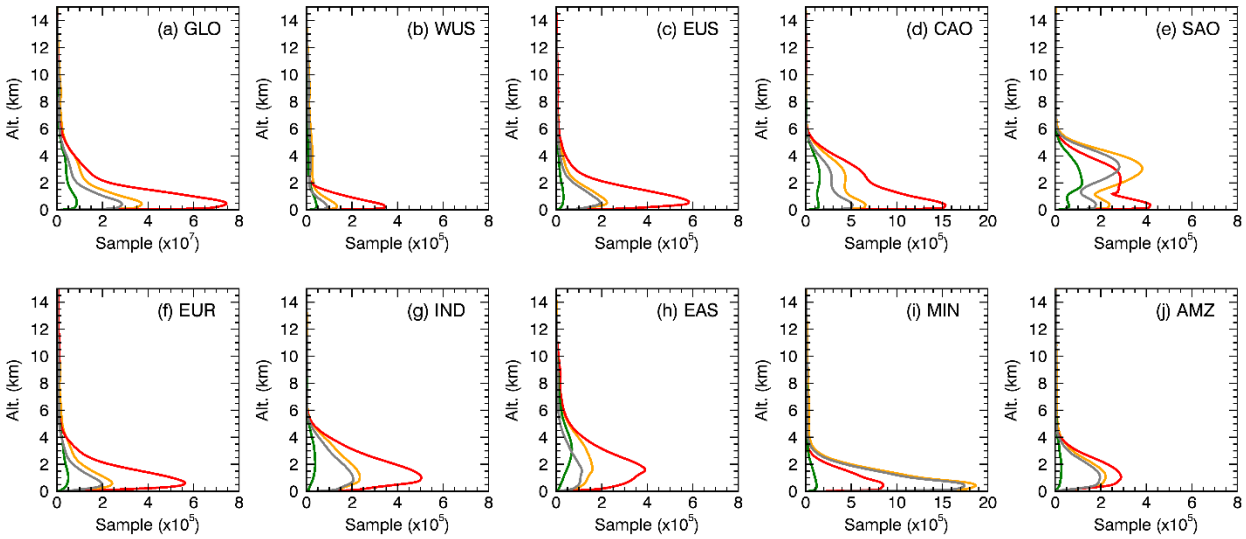

Figure 13. Same as Figure 11 but for vertical profiles of samples.

Similarly, over the Center Atlantic Ocean region (Figures 11-14d), aerosols originated from Africa dust are often elevated and transported westward (Yang et al., 2012). As displayed in Figures 13d and 14d, aerosols are concentrated in the boundary layer below 2 km but with another pump between 2-6 km. In this region, the cloud-free aerosols account for more than 50% through the year with no obvious seasonal cycles. However, the connected-cloud aerosol fraction displays seasonal periodicity that relates to the cumulus which appear from Mach – August each year (Figure 11d) (King et al., 2013). The timeseries of both the cloud-free and cloudy $\bar{\tau}_a$overlaps well, being larger in boreal summer season (Figure 12d) that is associated with the outbreak of Saharan air layer (Xian et al., 2020).

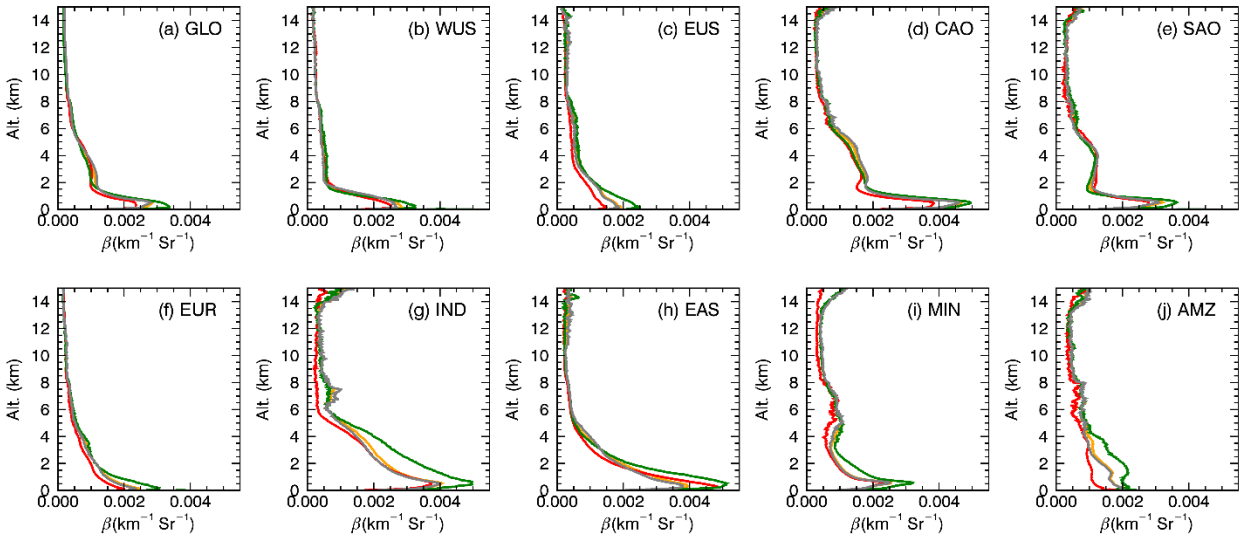

Figure 14. Same as Figure 11 but for profiles of the median values of lidar backscatters at 532 nm.

In the East Asian and Indian regions, aerosol characteristics are impacted by the Asian monsoon. The cloud-free aerosols occupy a higher fraction than the cloudy aerosols during the winter monsoon season in both regions, and vice versa during the summer monsoon season (Figures 11g and 11h). In the Indian region, $\bar{\tau}_a$ peaks in summer as the prevailing Southwest surface wind transports dust particles from the desert from Asia and Africa to India and its surrounding regions (Sivaprasad & Babu, 2014). The cloud-free τ_a is generally larger than the connected-cloud $\bar{\tau}_a$, while the isolated-cloud $\bar{\tau}_a$ is the smallest (Figure 12g). In East Asia, the connected-cloud aerosols are more prevalent during winter-spring season associating with the occurrence of the prevailing low stratiform clouds (Hong & Di Girolamo, 2020; Klein & Hartmann, 1993), while the isolated-cloud aerosols (primary below-cloud aerosol,) are being more frequent in summer (Figure 11h). Similar to Indian region, the cloud-free $\bar{\tau}_a$ is larger than the cloudy $\bar{\tau}_a$ as well, with the connected-cloud $\bar{\tau}_a$ being the smallest. In both regions, aerosols are detected up to 6 km (Figures 13g and 13h), whereas in India, aerosol backscatters are large up to 6 km and in East Asia, they decrease quicky above 2 km (Figures 14g and 14h).

In the other four regions- Europe (Figures 11f-14f), West of US (Figures 11b-14b), East US (Figures 11c-14c) and Amazon (Figures 11j-14j), the seasonal variations and the behaviors of the cloud-free and the cloudy aerosols also heavily rely on local weather and climate. For instance, in the Amazonian regions, the $\bar{\tau}_a$ and $\bar{f}_a$ peak in the dry season, and cloudy aerosols are dominated by the below-cloud aerosols (> 40%, Figure 6) due to ubiquitous cirrus; In the West of US, aerosols are detected below 2 km and rare aerosols are elevated above boundary layer, while in Europe, East US and Amazon, aerosols can be detected up to 4 km.

Overall, the characteristics of the cloud-free and the cloudy aerosols as well as their seasonal variations significantly vary with regions. In some regions such as in East Asia, the cloud-free $\bar{\tau}_a$ tends to be the largest, while in some other regions such as in Malaysia-Indonesia region, the cloud-free $\bar{\tau}_a$ is the smallest. The difference in the cloudy and the cloud-free $\bar{\tau}_a$ in a region relies on their differences in aerosol types, geometrical thickness of the aerosol layers as well as the retrieved τ_a uncertainties. One should be noted that the geometrical thickness of

aerosol layers is overall larger in clear sky than in cloudy sky, which should result in larger cloud-free $\bar{\tau}_a$. This is observed when the aerosol concentration is heavy such as in the Southeast Atlantic Ocean and Indian region. However, aerosol-cloud interactions and the larger $\bar{\tau}_a$ uncertainties in cloudy sky could also contribute to a larger cloudy $\bar{\tau}_a$. This can be revealed in Figure 12 when the aerosol concentration is low ($\bar{\tau}_a$ < 0.2), the cloudy $\bar{\tau}_a$ tends to be larger than the cloud-free $\bar{\tau}_a$. To what degree is contributed by aerosol-cloud interaction or retrieval uncertainty is not inferred in this study.

Regardless of regional τ_a differences, there are some common features. The median lidar backscatter profiles of the cloudy and the cloud-free aerosols are almost overlapped in all regions. However, the connected-cloud median backscatter profiles are the largest among all aerosol groups for all regions. The larger lidar backscatter of the connected-cloud aerosols could result from an enhancement of aerosol backscatter near cloud edge (Tackett & Di Girolamo, 2009). Misclassification of clouds, especially cloud detrainments near cloud boundary, to aerosols likely induce larger lidar backscatter to the connected-cloud aerosols as well.

5. Summary

This study examines the climatological properties of aerosols detected by CALIOP occurring in cloud-free and cloudy skies. Considering that clouds above or below aerosol layers influence aerosol direct radiative effects in a different way, cloudy aerosols are further classified into the connected-cloud and the isolated-cloud aerosols based on the vertically relative locations of aerosol and cloud layers. The differences between the cloud-free and the cloudy aerosols are emphasized by examining their spatial distributions, optical property, seasonal and regional variations.

Overall, for all the detected aerosols by CALIOP that pass our quality filters, the cloud-free aerosol samples account for about 55.9%, and the cloudy aerosol samples occupy about 44.1% over the globe. The cloudy aerosol samples are underestimated as CALIOP misses very thin aerosols and aerosols under opaque clouds. The global average optical depth ($\bar{\tau}_a$) and its uncertainty of the cloud-free and the cloudy aerosols are 0.135 ± 0.047 and 0.143 ± 0.074, respectively. The connected-cloud aerosols, occurring frequently in the marine stratocumulus and East Asian regions, have a $\bar{\tau}_a$ ~ 0.138 ± 0.063. The below-cloud aerosols, frequently occur in the regions covered by ubiquitous cirrus, have a $\bar{\tau}_a$ ~ 0.165 ± 0.087, whereas the above-cloud aerosols tend to have smaller $\bar{\tau}_a$ ~ 0.056 ± 0.039.

The cloud-free, the below-cloud, the one-layer aerosol-cloud connected and the aerosol-cloud connected layer below cloud layer aerosols primarily consist of marine aerosols, while the aerosol-cloud connected layer above cloud layer and the above-cloud aerosols contain more elevated smoke, polluted dust and volcano ash aerosols. We find similar τ_a PDFs, $\beta - \sigma$ and $Sr - \gamma$ diagrams between the one-layer aerosol-cloud connected and the aerosol-cloud connected layer below cloud layer aerosols, as well as between the below-cloud and the cloud-free aerosols. These similarities may indicate that the aerosol climatology from passive sensors may be well representative globally. However, considering the additional uncertainties caused by the overlying cloud layers to the underlying aerosols observed from space-borne lidar, it is necessary to utilize ground-based lidar observations to confirm the property similarity of aerosols with and without cloud layers above.

Also, this study reveals a wide coverage of the below-cloud aerosols that are frequently distributed over the tropical regions, which account for about ~ 21.2% among all detected

aerosols. Due to the fact that a cirrus layer is able to modify aerosol direct radiative effect at the TOA and heating rates in the atmosphere, it is important to quantify to what degree cirrus clouds change the underlying aerosol direct effect in order to obtain an accurate estimate of Earth radiation budget. The ground-based observations such as from the Atmospheric Radiation Measurement providing important measurements of clouds, aerosols and radiation will serve for simulating and constraining aerosol direct radiative effect at the TOA in both clear and cloudy skies regionally as demonstrated in two recent studies (Balmes & Fu, 2021; Wu et al., 2021).

Our results also suggest that regional and seasonal variations of the cloud-free and the cloudy aerosol fraction and optical depth are strong, which are affected by local emissions and large-scale climate systems. In East Asia and Southeast Atlantic Ocean, the cloud-free $\bar{\tau}_a$ is the largest, and the connected-cloud $\bar{\tau}_a$ is the smallest, vice versa in East US, West US and Malaysia-Indonesia regions. Though aerosol variations are huge in different regions. The connected-cloud lidar backscatter profiles (median values) are the largest among different aerosol groups in all selected regions. As aerosol and cloud layers are vertically adjunct, aerosol properties can be affected by clouds- hygroscopic aerosols might grow in a more humid environment near clouds (Rauber et al., 2013). Detrainment/entrainment cloud process could also alter aerosol properties Also, small cloud segments near cloud boundary also post challenges for the aerosol-cloud discrimination, leading to some cloudy pixels being identified as aerosols. To what degree the cloud contamination contributes to the connected-cloud profile is unknow.

Finally, this study has provided a comprehensive analysis of the cloud-free and the cloudy aerosols, which will aid the understanding and better quantifying the Earth radiation budget.

Acknowledgements

This research has been funded by the NASA CAMP^{2}Ex (Cloud, Aerosol and Monsoon Processes-Philippines Experiment) field campaign under the research grant 80NSSC18K0144 and 80NSSC21K1449. We acknowledge the CALIPSO science team for providing the aerosol products, which is available at https://search.earthdata.nasa.gov/search.

References

Alfaro-Contreras, R., Zhang, J., Campbell, J. R., & Reid, J. S. (2016). Investigating the frequency and interannual variability in global above-cloud aerosol characteristics with CALIOP and OMI. *Atmospheric Chemistry and Physics*, *16*(1), 47–69. https://doi.org/10.5194/acp-16-47-2016

Andreae, M. O., & Rosenfeld, D. (2008). Aerosol-cloud-precipitation interactions. Part 1. The nature and sources of cloud-active aerosols. *Earth-Science Reviews*, *89*(1–2), 13–41. https://doi.org/10.1016/j.earscirev.2008.03.001

Balmes, K. A., & Fu, Q. (2021). All-Sky Aerosol Direct Radiative Effects at the ARM SGP Site. *Journal of Geophysical Research: Atmospheres*, *126*(17). https://doi.org/10.1029/2021JD034933

Burton, S. P., Ferrare, R. A., Hostetler, C. A., Hair, J. W., Rogers, R. R., Obland, M. D., et al. (2012). Aerosol classification using airborne High Spectral Resolution Lidar measurements-

methodology and examples. *Atmospheric Measurement Techniques*, *5*(1), 73–98. https://doi.org/10.5194/amt-5-73-2012

Chand, D., Wood, R., Anderson, T. L., Satheesh, S. K., & Charlson, R. J. (2009). Satellite-derived direct radiative effect of aerosols dependent on cloud cover. *Nature Geoscience*, *2*(3), 181–184. https://doi.org/10.1038/ngeo437

Christensen, M. W., & Stephens, G. L. (2011). Microphysical and macrophysical responses of marine stratocumulus polluted by underlying ships: Evidence of cloud deepening. *Journal of Geophysical Research Atmospheres*, *116*(3), 1–10. https://doi.org/10.1029/2010JD014638

Chung, C. E., Lewinschal, A., & Wilcox, E. (2016). Relationship between low-cloud presence and the amount of overlying aerosols. *Atmospheric Chemistry and Physics*, *16*(9), 5781–5792. https://doi.org/10.5194/acp-16-5781-2016

Devasthale, A., & Thomas, M. A. (2011). A global survey of aerosol-liquid water cloud overlap based on four years of CALIPSO-CALIOP data. *Atmospheric Chemistry and Physics*, *11*(3), 1143–1154. https://doi.org/10.5194/acp-11-1143-2011

Grythe, H., Ström, J., Krejci, R., Quinn, P., & Stohl, A. (2014). A review of sea-spray aerosol source functions using a large global set of sea salt aerosol concentration measurements. *Atmospheric Chemistry and Physics*, *14*(3), 1277–1297. https://doi.org/10.5194/acp-14-1277-2014

Ten Hoeve, J. E., & Augustine, J. A. (2016). Aerosol effects on cloud cover as evidenced by ground-based and space-based observations at five rural sites in the United States. *Geophysical Research Letters*, *43*(2), 793–801. https://doi.org/10.1002/2015GL066873

Hong, Y., & Di Girolamo, L. (2020). Cloud Phase Characteristics Over Southeast Asia from A-Train Satellite Observations. *Atmospheric Chemistry and Physics*, (20), 8267–8291. https://doi.org/https://doi.org/10.5194/acp-20-8267-2020

Hong, Y., & Liu, G. (2015). The characteristics of ice cloud properties derived from CloudSat and CALIPSO measurements. *Journal of Climate*, *28*, 3880–3901. https://doi.org/10.1175/JCLI-D-14-00666.1

IPCC. (2021). *Climate Change 2021: The Physical Science Basis. Contribution of Working Group I to the Sixth Assessment Report of the Intergovernmental Panel on Climate Change*. Cambridge University Press.

Keil, A., & Haywood, J. M. (2003). Solar radiative forcing by biomass burning aerosol particles during SAFARI 2000: A case study based on measured aerosol and cloud properties. *Journal of Geophysical Research: Atmospheres*, *108*(13), 1–10. https://doi.org/10.1029/2002jd002315

Kim, M.-H., Omar, A. H., Tackett, J. L., Vaughan, M. A., Winker, D. M., Trepte, C. R., et al. (2018). The CALIPSO version 4 automated aerosol classificaiton and lidar ratio selection algorithm. *Atmospehric Measurment Techniques*, *11*, 6107–6135. https://doi.org/10.5194/amt-11-6107-2018

Kim, S. W., Yoon, S. C., Kim, J., & Kim, S. Y. (2007). Seasonal and monthly variations of

columnar aerosol optical properties over east Asia determined from multi-year MODIS, LIDAR, and AERONET Sun/sky radiometer measurements. *Atmospheric Environment*, *41*(8), 1634–1651. https://doi.org/10.1016/j.atmosenv.2006.10.044

King, M. D., Platnick, S., Menzel, W. P., Ackerman, S. A., & Hubanks, P. A. (2013). Spatial and temporal distribution of clouds observed by MODIS onboard the Terra and Aqua satellites. *IEEE Transactions on Geoscience and Remote Sensing*, *51*, 3826–3852. https://doi.org/10.1109/TGRS.2012.2227333

Klein, S. A., & Hartmann, D. L. (1993). The seasonal cycle of low stratiform clouds. *Journal of Climate*. https://doi.org/10.1175/1520-0442(1993)006<1587:TSCOLS>2.0.CO;2

Lebsock, M. D., Stephens, G. L., & Kummerow, C. (2008). Multisensor satellite observations of aerosol effects on warm clouds. *Journal of Geophysical Research Atmospheres*, *113*(15), 1–12. https://doi.org/10.1029/2008JD009876

Liao, H., & Seinfeld, J. H. (1998). Effect of clouds on direct aerosol radiative forcing of climate. *Journal of Geophysical Research Atmospheres*, *103*(D4), 3781–3788. https://doi.org/10.1029/97JD03455

Liu, Z., Vaughan, M., Winker, D., Kittaka, C., Getzewich, B., Kuehn, R., et al. (2009). The CALIPSO lidar cloud and aerosol discrimination: Version 2 algorithm and initial assessment of performance. *Journal of Atmospheric and Oceanic Technology*, *26*(7), 1198–1213. https://doi.org/10.1175/2009JTECHA1229.1

Liu, Z., Kar, J., Zeng, S., Tackett, J., Vaughan, M., Avery, M., et al. (2019). Discriminating between clouds and aerosols in the CALIOP version 4 . 1 data products, *2006*, 703–734.

Loeb, N. G., & Manalo-Smith, N. (2005). Top-of-atmosphere direct radiative effect of aerosols over global oceans from merged CERES and MODIS observations. *Journal of Climate*, *18*(17), 3506–3526. https://doi.org/10.1175/JCLI3504.1

Lohmann, U., & Feichter, J. (2005). Global indirect aerosol effects: a review. *Atmos. Chem. Phys*, *5*, 715–737. https://doi.org/10.5194/acp-5-715-2005

Mao, K. B., Ma, Y., Xia, L., Chen, W. Y., Shen, X. Y., He, T. J., & Xu, T. R. (2014). Global aerosol change in the last decade: An analysis based on MODIS data. *Atmospheric Environment*, *94*, 680–686. https://doi.org/10.1016/j.atmosenv.2014.04.053

Matus, A. V., L'Ecuyer, T. S., Kay, J. E., Hannay, C., & Lamarque, J.-F. (2015). The role of clouds in modulating global aerosol direct radiative effects in spaceborne active observations and the community earth system model. *Journal of Climate*, *28*(8), 2986–3003. https://doi.org/10.1175/JCLI-D-14-00426.1

Mehta, M., Singh, R., Singh, A., Singh, N., & Anshumali. (2016). Recent global aerosol optical depth variations and trends - A comparative study using MODIS and MISR level 3 datasets. *Remote Sensing of Environment*, *181*, 137–150. https://doi.org/10.1016/j.rse.2016.04.004

Mishchenko, M. I., Geogdzhayev, I. V., Cairns, B., Carlson, B. E., Chowdhary, J., Lacis, A. A., et al. (2007). Past, present, and future of global aerosol climatologies derived from satellite observations: A perspective. *Journal of Quantitative Spectroscopy and Radiative Transfer*, *106*(1–3), 325–347. https://doi.org/10.1016/j.jqsrt.2007.01.007

Omar, A. H., Winker, D. M., Kittaka, C., Vaughan, M. A., Liu, Z., Hu, Y., et al. (2009). The CALIPSO automated aerosol classification and lidar ratio selection algorithm. *Journal of Atmospheric and Oceanic Technology*, *26*(10), 1994–2014. https://doi.org/10.1175/2009JTECHA1231.1

Palacios-Penã, L., Jiménez-Guerrero, P., Baró, R., Balzarini, A., Bianconi, R., Curci, G., et al. (2019). Aerosol optical properties over Europe: An evaluation of the AQMEII Phase 3 simulations against satellite observations. *Atmospheric Chemistry and Physics*, *19*(5), 2965–2990. https://doi.org/10.5194/acp-19-2965-2019

Rauber, R. M., Zhao, G., Girolamo, L. Di, & Colón-Robles, M. (2013). Aerosol size distribution, particle concentration, and optical property variability near caribbean trade cumulus clouds: Isolating effects of vertical transport and cloud processing from humidification using aircraft measurements. *Journal of the Atmospheric Sciences*, *70*(10), 3063–308. https://doi.org/10.1175/JAS-D-12-0105.1

Remer, L. A., Kleidman, R. G., Levy, R. C., Kaufman, Y. J., Tanré, D., Mattoo, S., et al. (2008). Global aerosol climatology from the MODIS satellite sensors. *Journal of Geophysical Research Atmospheres*, *113*(14), 1–18. https://doi.org/10.1029/2007JD009661

Rosenfeld, D., Andreae, M. O., Asmi, A., Chin, M., Leeuw, G., Donovan, D. P., et al. (2014). Global observations of aerosol-cloud-precipitation- climate interactions. *Reviews of Geophysics*, *52*, 750–808. https://doi.org/10.1002/2013RG000441

Rosenfeld, D., Zhu, Y., Wang, M., Zheng, Y., Goren, T., & Yu, S. (2019). Aerosol-driven droplet concentrations dominate coverage and water of oceanic low-level clouds. *Science*, *363*(6427), eaav0566. https://doi.org/10.1126/science.aav0566

Ross, A. D., Holz, R. E., Quinn, G., Reid, J. S., Xian, P., Joseph Turk, F., & Posselt, D. J. (2018). Exploring the first aerosol indirect effect over Southeast Asia using a 10-year collocated MODIS, CALIOP, and model dataset. *Atmospheric Chemistry and Physics*, *18*, 12747–12764. https://doi.org/10.5194/acp-18-12747-2018

Sassen, K., & Wang, Z. (2008). Classifying clouds around the globe with the CloudSat radar: 1-year of results. *Geophysical Research Letters*, *35*, L04805. https://doi.org/10.1029/2007GL032591

Sassen, K., Wang, Z., & Liu, D. (2008). Global distribution of cirrus clouds from CloudSat/Cloud-Aerosol Lidar and Infrared Pathfinder Satellite Observations (CALIPSO) measurements. *Journal of Geophysical Research*, *113*, D00A12. https://doi.org/10.1029/2008JD009972

Shinozuka, Y., Kacenelenbogen, M., Burton, S., Howell, S., Zuidema, P., Ferrare, R., et al. (2020). Daytime aerosol optical depth above low-level clouds is similar to that in adjacent clear skies at the same heights: airborne observation above the southeast Atlantic. *Atmospheric Chemistry and Physics*, (January), 1–26. https://doi.org/10.5194/acp-2019-1007

Sivaprasad, P., & Babu, C. A. (2014). Seasonal variation and classification of aerosols over an inland station in India. *Meteorological Applications*, *21*(2), 241–248. https://doi.org/10.1002/met.1319

Tackett, J. L., & Di Girolamo, L. (2009). Enhanced aerosol backscatter adjacent to tropical trade wind clouds revealed by satellite-based lidar. *Geophysical Research Letters*, *36*(14), 1–5. https://doi.org/10.1029/2009GL039264

Tackett, Jason L., Winker, D. M., Getzewich, B. J., Vaughan, M. A., Young, S. A., & Kar, J. (2018). CALIPSO lidar level 3 aerosol profile product: Version 3 algorithm design. *Atmospheric Measurement Techniques*, *11*(7), 4129–4152. https://doi.org/10.5194/amt-11-4129-2018

Tan, S., Han, Z., Wang, B., & Shi, G. (2017). Variability in the correlation between satellite-derived liquid cloud droplet effective radius and aerosol index over the northern Pacific Ocean. *Tellus B: Chemical and Physical Meteorology*, *69*(1), 1391656. https://doi.org/10.1080/16000889.2017.1391656

Vaughan, M. A., Powell, K. A., Kuehn, R. E., Young, S. A., Winker, D. M., Hostetler, C. A., et al. (2009). Fully automated detection of cloud and aerosol layers in the CALIPSO lidar measurements. *Journal of Atmospheric and Oceanic Technology*, *26*(10), 2034–2050. https://doi.org/10.1175/2009JTECHA1228.1

Winker, D. M., Tackett, J. L., Getzewich, B. J., Liu, Z., Vaughan, M. A., & Rogers, R. R. (2013). The global 3-D distribution of tropospheric aerosols as characterized by CALIOP. *Atmospheric Chemistry and Physics*, *13*(6), 3345–3361. https://doi.org/10.5194/acp-13-3345-2013

Winker, David M., Pelon, J. R., & McCormick, M. P. (2003). The CALIPSO mission: Spaceborne lidar for observation of aerosols and clouds. *Lidar Remote Sensing for Industry and Environment Monitoring III*, *4893*, 1–11. https://doi.org/10.1117/12.466539

Winker, David M., Vaughan, M. A., Omar, A., Hu, Y., Powell, K. A., Liu, Z., et al. (2009). Overview of the CALIPSO mission and CALIOP data processing algorithms. *Journal of Atmospheric and Oceanic Technology*, *26*(11), 2310–2323. https://doi.org/10.1175/2009JTECHA1281.1

Wu, X., Balmes, K. A., & Fu, Q. (2021). Aerosol Direct Radiative Effects at the ARM SGP and TWP Sites: Clear Skies. *Journal of Geophysical Research: Atmospheres*, *126*(5), 1–24. https://doi.org/10.1029/2020JD033663

Xian, P., Klotzbach, P., Dunion, J., Janiga, M., Reid, J., Colarco, P., & Kipling, Z. (2020). Revisiting the relationship between Atlantic dust and tropical cyclone activity using aerosol optical depth reanalyses: 2003–2018. *Atmospheric Chemistry and Physics*, 1–43. https://doi.org/10.5194/acp-2020-287

Xu, H., Guo, J., Wang, Y., Zhao, C., Zhang, Z., Min, M., et al. (2017). Warming effect of dust aerosols modulated by overlapping clouds below. *Atmospheric Environment*, *166*, 393–402. https://doi.org/10.1016/j.atmosenv.2017.07.036

Yang, W., Marshak, A., Várnai, T., Kalashnikova, O. V., & Kostinski, A. B. (2012). CALIPSO observations of transatlantic dust: Vertical stratification and effect of clouds. *Atmospheric Chemistry and Physics*, *12*(23), 11339–11354. https://doi.org/10.5194/acp-12-11339-2012

Young, S. A., & Vaughan, M. A. (2009). The retrieval of profiles of particulate extinction from

cloud-aerosol lidar infrared pathfinder satellite observations (CALIPSO) data: Algorithm description. *Journal of Atmospheric and Oceanic Technology*, *26*(6), 1105–1119. https://doi.org/10.1175/2008JTECHA1221.1

Young, S. A., Winker, D. M., Hu, Y., & Kuehn, R. E. (2008). CALIOP algorithm theoretical basis document, Part 4: Extinction retrieval algorithms. *Theoretical Basis Documents*. Retrieved from http://scholar.google.com/scholar?hl=en&btnG=Search&q=intitle:CALIOP+Algorithm+Theoretical+Basis+Document+Part+3+:+Scene+Classification+Algorithms#0

Young, S. A., Vaughan, M. A., Kuehn, R. E., & Winker, D. M. (2013). The retrieval of profiles of particulate extinction from Cloud-Aerosol Lidar and Infrared Pathfinder Satellite Observations (CALIPSO) data: Uncertainty and error sensitivity analyses. *Journal of Atmospheric and Oceanic Technology*, *30*(3), 395–428. https://doi.org/10.1175/JTECH-D-12-00046.1

Zhang, Z., Meyer, K., Yu, H., Platnick, S., Colarco, P., Liu, Z., & Oreopoulos, L. (2016). Shortwave direct radiative effects of above-cloud aerosols over global oceans derived from 8 years of CALIOP and MODIS observations. *Atmospheric Chemistry and Physics*, *16*(5), 2877–2900. https://doi.org/10.5194/acp-16-2877-2016